Advanced Materials

ADVANCED MATERIALS
www.advmat.de

RESEARCH ARTICLE

Dual Oxygen Precursors Boosting the Ionic Conductivity of Glassy Electrolytes for All-Solid-State Sodium Batteries

Lihao Tang[1,2] | Liwei Jiang[3] | Yang Huang[3] | Rui Bai[1,2] | Jingchen Lian[1,2] | Haibo Wang[1,4] | Hao Jiang[1,2] | Bowen Wang[1,4] | Xubin Wang[1,4] | Yuyao Wang[1,4] | Jian Peng[5] | Fei Xie[1,4] | Xiaohui Rong[1,4] | Liquan Chen[1] | Yong-Sheng Hu[1,4] | Yaxiang Lu[1,6]

[1]Key Laboratory for Renewable Energy, Institute of Physics, Chinese Academy of Sciences, Beijing, China | [2]College of Physical Sciences, University of Chinese Academy of Sciences, Beijing, China | [3]CAS Key Laboratory of Green Process and Engineering, Institute of Process Engineering, Chinese Academic of Sciences, Beijing, China | [4]College of Materials Science and Optoelectronic Technology, University of Chinese Academy of Sciences, Beijing, China | [5]Zhejiang Key Laboratory of All-Solid-State Battery, Eastern Institute of Technology, Ningbo, China | [6]Huairou Division, Institute of Physics, Chinese Academy of Sciences, Beijing, China

Correspondence: Yaxiang Lu (yxlu@iphy.ac.cn)

Received: 10 April 2026 | **Revised:** 7 July 2026 | **Accepted:** 24 July 2026

Keywords: deoxygenation enthalpy | halide electrolyte | oxygen source | solid-state Na battery | viscoelastic inorganic glass

ABSTRACT

Amorphous halide-based solid electrolytes (SEs) are promising candidates for all-solid-state Na batteries (ASSNaBs) due to their structural flexibility and favorable mechanical properties. Among them, aluminum-based halide electrolytes are particularly attractive owing to their low cost and oxidative stability; however, previously reported systems typically exhibit limited room-temperature ionic conductivity (<1 mS cm^{-1}). In this work, we report the synthesis of a transparent, viscoelastic Na–Al SE with the specific composition $0.6NaClO–AlCl_3–0.175SeO_2$, achieved through the strategic introduction of dual oxygen sources (NaClO and SeO_2). This approach enables the modulation of charge carrier concentrations while simultaneously supplying sufficient oxygen. Furthermore, we introduce the concept of deoxygenation enthalpy to rationalize the selection of these dual oxygen sources among various oxide candidates. The resulting electrolyte achieves a high Na^+ conductivity of 2.03 mS cm^{-1} at ambient temperatures, among the highest reported for Na–Al halide electrolytes. Molecular dynamics simulations confirm that segmental motion within the disordered framework actively facilitates Na^+ transport, underpinning the observed viscoelastic behavior. When integrated into ASSNaB with uncoated $NaNi_{0.4}Fe_{0.2}Mn_{0.4}O_2$ cathode, the electrolyte enables stable long-term cycling and superior thermal compatibility, demonstrating practical applicability. This work establishes a new paradigm in rational precursor design for high-performance viscoelastic SEs.

1 | Introduction

All-solid-state Na batteries (ASSNaBs) represent a promising pathway toward safe, high-energy-density energy storage, with solid electrolytes (SEs) dictating their ultimate performance. However, simultaneous realization of high ionic conductivity, mechanical deformability, and robust interfacial compatibility remains a significant challenge [1], particularly for Na^+-conducting systems. Crystalline halide SEs, despite their good oxidative stability and processability [2], are intrinsically ill-suited for Na^+ transport due to rigid lattices, low coordination numbers, and narrow diffusion bottlenecks [3], which impose

Lihao Tang and Liwei Jiang contributed equally to this work.

high activation barriers and severely limit room-temperature ionic conductivity [4, 5]. These limitations have spurred interest in amorphous halides, where structural disorder can open wider ion-conduction pathways [6–8].

Aluminum-based halide electrolytes have attracted growing interest due to their low cost, compositional tunability, and compatibility with high-voltage cathodes. Following our group's discovery of a viscoelastic aluminum oxychloride electrolyte [9], research on $AlCl_3$-derived systems has expanded rapidly across both Li- and Na-ion chemistries. A common strategy involves incorporating oxygen from various precursors, such as Li_2O_2 [10], hydrated salts ($AlCl_3{\cdot}6H_2O$) [11], carbonates (Na_2CO_3) [12], or metal oxides (Sb_2O_3) [13], to disrupt long-range order and enhance ion mobility (Table S1). While oxygen doping effectively promotes amorphization and boosts conductivity [14, 15], a critical shortcoming remains. Nearly all reported Al-based amorphous SEs are rigid powders, lacking the viscoelasticity required for conformal electrode-electrolyte contact and strain accommodation during cycling. Moreover, reliance on a single oxygen source often fails to fully saturate the Al^{3+} coordination sphere or establish a continuous percolating Al–O–Al network, a prerequisite for simultaneously achieving high ionic conductivity and mechanical compliance. This limitation led us to question whether a single oxygen precursor could ever provide the right balance of oxygen quantity, reactivity, and release kinetics. We recognized that oxygen donors vary not only in oxygen content but also in thermodynamic stability and kinetic behavior during reaction with metal halides. To harness these differences, we introduce a paradigm-shifting dual-oxygen-precursor strategy, classifying donors into two categories: "Salt-Oxygen" (SO) and "Metal/Non-metal Oxide-Oxygen" (M/NO). SO precursors, such as NaClO, readily release reactive oxygen at low temperatures, enabling rapid initiation of the oxyhalide network and serving concurrently as the sole Na^+ source, a Cl^- contributor, and an initial O^{2-} donor. In contrast, M/NO sources like SeO_2 require higher activation energy but provide controlled, delayed oxygen release, which refines the local coordination environment and completes the bridging network.

Herein, we report a new class of sodium-conducting SEs, denoted as NACDO (Na-Al-Cl-Dual-Oxygen), with the general composition $0.6NaClO–AlCl_3–xO$ ($25\% \leq x \leq 45\%$). These materials are synthesized via a facile one-step, low-temperature (300°C–400°C) rapid sintering process completed within 0.5 h. The deliberate use of sub-stoichiometric NaClO (0.6 eq.) induces sodium deficiency, which provides sufficient charge carriers while suppressing parasitic NaCl crystallization, thereby enhancing ionic transport. However, NaClO alone cannot supply sufficient oxygen to form a fully connected Al–O–Al framework. The addition of SeO_2 as a complementary M/NO source bridges this gap, enabling the formation of a transparent, fully amorphous, and viscoelastic oxyhalide network stabilized by both bridging and non-bridging oxygen species. This rationally engineered architecture delivers exceptional properties: a room-temperature Na^+ conductivity of 2.03 mS cm^{-1}, an electrochemical stability window up to 4.4 V versus $Na^+/Na_{15}Sn_4$, negligible electronic conduction ($<10^{-8}$ S cm^{-1}), and excellent interfacial compatibility with oxide cathodes. When integrated directly with an uncoated layered oxide cathode ($NaNi_{0.4}Fe_{0.2}Mn_{0.4}O_2$), the resulting ASSNaB retains >80% of its initial capacity after 480 cycles at 0.3 C, significantly outperforming all previously reported Al-based sodium electrolytes. Beyond this materials breakthrough, our work establishes a generalizable SO-M/NO precursor design framework for rational oxygen incorporation—applicable to other metal halide systems such as $TaCl_5$ and $InBr_3$, thereby bridging the long-standing gap between high ionic conductivity and mechanical compliance in SEs for next-generation ASSNaBs.

2 | Dual-Oxygen Precursor Strategy for Viscoelastic Al-Based SEs

In contrast to the time-intensive and energy-intensive ball-milling method, low-temperature rapid sintering enables an enhancement in experimental efficiency (Figure 1a). The rational design of our Al-based SEs commenced with the strategic selection of sodium hypochlorite (NaClO) as a primary precursor, chosen specifically for its capability to simultaneously supply both chlorine and oxygen within a single molecular unit. Unlike conventional syntheses that rely on discrete sodium salts containing solely oxygen (e.g., Na_2O, Na_2O_2, Na_2CO_3) [12, 16, 17], chlorine (NaCl) [18], or hydroxide (NaOH) [19, 20], where disparities in bond strengths often complicate low-temperature melting kinetics. To address this, NaClO is utilized as a unified source for both anions. This dual-element nature was hypothesized to be critical for inducing structural disorder while maintaining the necessary halide chemistry. Initial trials combining NaClO with $AlCl_3$ yielded the binary system NACO (Na-Al-Cl-O), which exhibited exceptional viscoelasticity and a high degree of amorphous disorder (Figure 1b). However, its ionic conductivity remained unsatisfactory (Figure S1). Optimization determined an NaClO dosage of 0.6 to be optimal. Attempts to adjust stoichiometry by adding excess NaCl led to saturation, material pulverization, reduced conductivity, and the reappearance of crystalline impurities (Figure S1). This indicated that while the simultaneous Cl/O supply from NaClO was excellent for creating an amorphous, viscoelastic matrix, it was insufficient on its own to establish a highly conductive ion-transport network. In contrast, electrolytes prepared with $NaAlCl_4$ and SeO_2 as the sole oxygen source exhibit intense diffraction peaks corresponding to crystalline NaCl (Figure S1). Meanwhile, they deliver low ionic conductivity and suffer from reduced optical transparency. To bridge this gap, we added SeO_2 as a secondary network former, engineering the ternary NACDO (Na-Al-Cl-Dual-Oxygen) series. Inspired by substitution chemistry in which chlorides volatilize to form oxygen bridges, we exploited the strong thermodynamic driving force of the reaction between $AlCl_4^-$ and SeO_2 to construct a robust amorphous framework. This synergistic strategy using NaClO and SeO_2 for concurrent Cl/O-induced disorder and network bridging is highly effective. Hereinafter, NACO refers to $0.6NaClO–AlCl_3$, and NACDO refers to $0.6NaClO–AlCl_3–0.175SeO_2$.

X-ray diffraction (XRD) analysis confirmed the success of this design. At optimal NaClO ratios and oxygen substitution levels, NACDO exhibited complete amorphization, displaying only broad diffuse peaks characteristic of a glassy state without any sharp crystalline signals (Figure 1c). Notably, no peaks corresponding to NaCl, unreacted $AlCl_3$, or the common by-product $NaAlCl_4$ were observed, even when XRD was conducted without

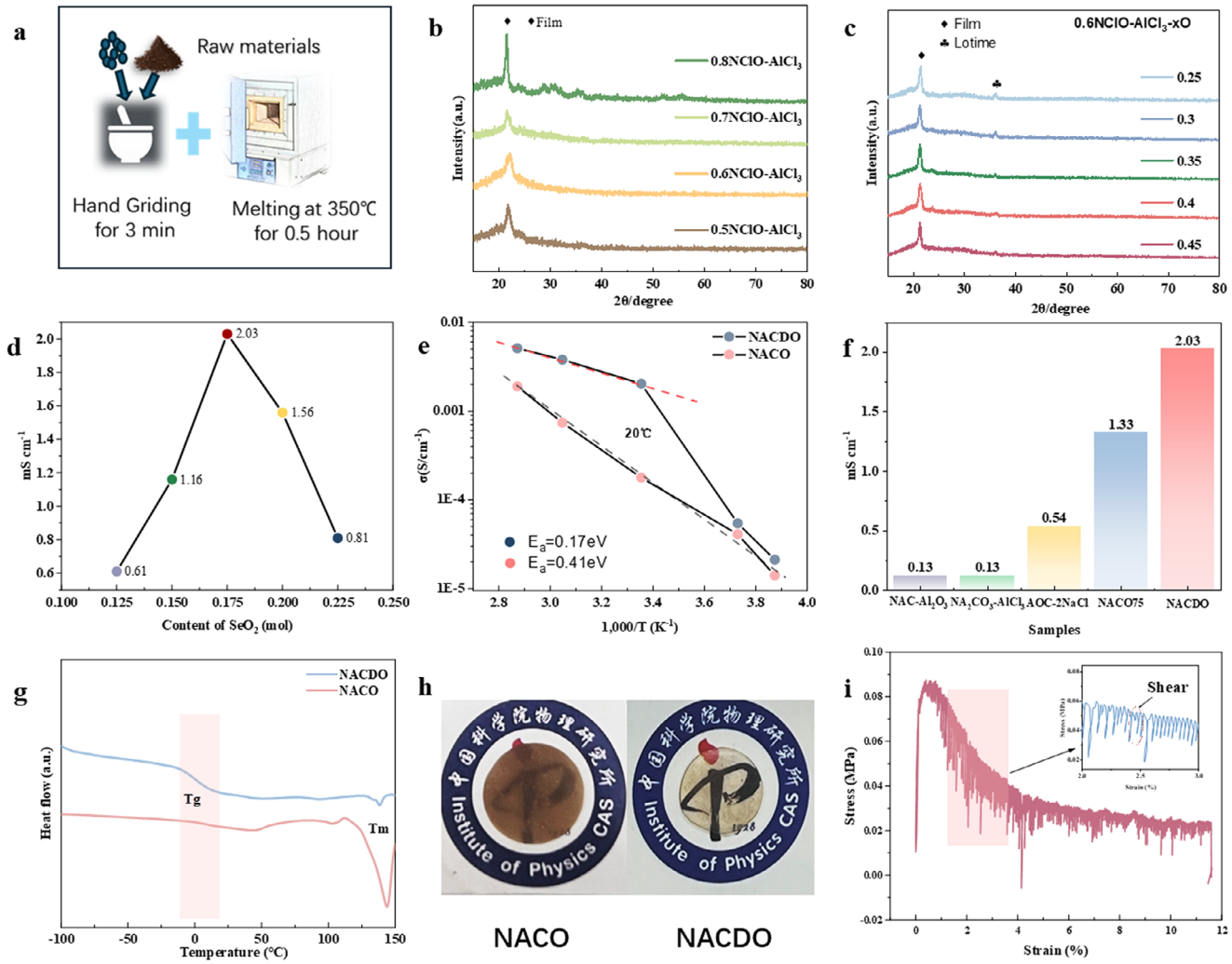

FIGURE 1 | (a) Simplified experimental flow diagram. (b, c) XRD spectra of SEs obtained without and with SeO_2 respectively, under the same synthesis conditions. (d) Ionic conductivity of NACDO with various SeO_2 amounts. (e) The temperature (T)-dependent ionic conductivities (σ) of the amorphous electrolytes. (f) Comparison of ionic conductivity of sodium-ion aluminum-based solid electrolytes [9, 12, 13, 26]. NACO75 refers to $NaAlCl_{2.5}O_{0.75}$. (g) Differential scanning calorimetry measurement of T_g and melting point T_m. (h) Diagram of optical transparency of aluminum-based solid electrolyte. (i) Stress–strain curve of NACDO at room temperature.

protective measures to rule out interference from vacuum grease or films (Figure S2). This stands in stark contrast to many reported amorphous halide electrolytes that suffer from excessive sodium halide impurity segregation [21–23]. Instead, NACDO achieves a homogeneous integration of sodium ions with Al and O species rather than isolated chloride phases. This structural homogeneity is not limited to aluminum, and the dual-oxygen strategy successfully extends to transition metal analogues (Ta, In, and Ga-based systems), all of which exhibit similar excellent amorphization and viscoelastic characteristics (Figure S3), validating the universality of this design principle.

Electrochemical impedance spectroscopy (EIS) revealed that NACDO achieves a record-high room-temperature (RT) ionic conductivity of 2.03 mS cm^{-1}, surpassing all previously reported Al-based sodium halide SEs (Figure 1d,f). The activation energy (E_a) of NACDO is lower than that of NACO, indicating fewer ion transport barriers. Furthermore, the material exhibits a high oxidative stability up to 4.4 V (vs. $Na^+/Na_{15}Sn_4$), ensuring excellent compatibility with high-voltage layered oxide cathodes (Figure S1). DC polarization measurements confirmed that NACDO is a pure ionic conductor, with negligible electronic conductivity ($< 10^{-8}$ S cm^{-1}) and a high Na^+ transference number of 0.87 (Figures S4 and S5). This characteristic effectively prevents short internal circuits and facilitates normal ionic transportation.

Beyond electrochemical metrics, NACDO possesses unique mechanochemical properties derived from its disordered but connected network. Surprisingly, both the binary NACO and ternary NACDO systems maintain viscoelasticity at room temperature, attributed to an exceptionally low glass transition temperature (T_g = −5°C). Unlike conventional Al-based electrolytes reported as rigid powders or clay-like aggregates, NACDO forms optically transparent, polymer-like solids (Figure 1h). This feature allows direct film formation without the need for grinding or high-pressure sintering; instead, thin films can be cast or pressed at mild conditions to form smooth, dense interfaces with cathode materials, as confirmed by scanning electron microscopy (SEM) and energy dispersive x-ray spectroscopy (EDS) elemental mapping (Figures S6 and S7). Mechanical testing further elucidated

the nature of this viscoelasticity. Stress-strain tensile tests on NACDO thin films revealed a distinct mechanical response: after a brief linear elastic region, the material exhibited frequent shear behavior rather than brittle fracture (Figure 1i). Thus, during practical mechanical testing, the strip specimens consistently exhibited extensive plastic deformation without catastrophic bulk fracture across the full sample. Micropillar compression tests corroborated this, showing a pronounced horizontal offset of the pillar top indicative of shear slip, a phenomenon commonly associated with amorphous alloys but rarely observed in inorganic salt electrolytes [24, 25] (Figure S8). The calculated Young's modulus of approximately 70 MPa highlights the material's softness and deformability. This unique combination of segmental mobility and shear plasticity suggests that the NACDO network can dynamically accommodate volume changes during battery cycling, ensuring sustained interfacial contact and mechanical integrity, a critical advantage over rigid ceramic electrolytes.

3 | Thermodynamic Control of Reactivity: The Deoxygenation Enthalpy Descriptor

To elucidate the fundamental reaction mechanisms driving the formation of viscoelastic electrolytes, we propose a dual-pathway substitution strategy centered on the nucleophilic attack of oxygen on $AlCl_3$. In the first pathway, oxygen atoms within the hypochlorite ion (ClO^-) of NaClO attack $AlCl_3$, substituting chlorine ligands and releasing free chloride ions (Cl^-). These Cl^- ions subsequently react with electrophilic chlorine species (Cl^+) to evolve volatile chlorine gas (Cl_2). Although previous in situ thermal decomposition experiments on halide electrolyte/oxide cathode mixtures under identical heating conditions detected only minor Cl evolution via mass spectrometry [27], this confirms that oxide-driven chlorine release is an intrinsic reaction pathway in halide systems. Since NaClO functions as a strong oxidant analogous to oxide cathodes, this prior evidence supports the proposed Cl_2 generation mechanism in the present NaClO-based synthesis. Concurrently, in the second pathway, oxygen from SeO_2 attacks the $AlCl_4^-$, displacing chlorine to generate Cl^- that coordinates with Se^{4+} to form volatile $SeCl_4$. To verify selenium volatilization, we analyzed the elemental composition of the final products using inductively coupled plasma optical emission spectroscopy (ICP-OES). These trace residual selenium content confirms near-complete volatilization of $SeCl_4$. Given that $SeCl_4$ has a boiling point of ~300°C and our synthesis temperature is maintained at 350°C, the minimal residual selenium provides strong indirect validation that $SeCl_4$ is fully volatilized as proposed (Table S2). Together, these volatilization events serve as entropic drivers that facilitate the removal of excess chlorine and the incorporation of oxygen bridges into the disordered aluminum network (Figure 2a).

Moreover, our experimental survey reveals that not all oxygen-containing precursors can undergo substitution reactions with $AlCl_3$ via low-temperature melting to yield room-temperature viscoelastic SEs. While substances such as Sb_2O_3, SeO_2, NaClO, and hydrated alums (e.g., $Al_2(SO_4)_3{\cdot}18H_2O$) successfully drive this transformation (Figure S9), many others fail (Figure S10). This selectivity raises a pivotal question: what governs the ability of a precursor to induce viscoelasticity? Our investigation identifies deoxygenation enthalpy (ΔH_{deox}) as the governing thermodynamic descriptor. Density functional theory (DFT) calculations reveal a direct correlation between ΔH_{deox} and reactivity: a lower ΔH_{deox} indicates a reduced energy barrier for oxygen dissociation, enabling active participation in the substitution at mild temperatures. Experimental validation confirms that sodium salts with ΔH_{deox} values below a critical threshold (~1 eV), specifically NaClO, $NaClO_2$, and $NaClO_4$, successfully transform $AlCl_3$ into viscoelastic, amorphous SEs (Figure S11). In contrast, we observe two distinct modes of inertness among other precursors. First, thermally stable salts (e.g., Na_3PO_4, Na_2SO_4, Na_2CO_3) maintain their intact anionic structures without decomposing to release free oxygen; while these anions may incorporate as functional groups, they do not act as primary oxygen donors for the viscoelastic transition. Second, refractory oxides (e.g., MgO, Al_2O_3, ZrO_2, Ta_2O_5), renowned for their wear- and heat-resistant properties, possess prohibitively high ΔH_{deox} values (Figure 2b). Their oxygen is tightly bound to dissociate under our synthesis conditions, rendering them kinetically inert. Consequently, reactions involving these stable salts or refractory oxides yield physical mixtures dominated by crystalline $NaAlCl_4$ rather than the desired amorphous phase (Figures S12). These findings necessitate a classification of precursors into "reactive oxygen donors" capable of direct substitution with $AlCl_3$ versus "inert frameworks" that typically yield crystalline powders dominated by $NaAlCl_4$ phases. By precisely targeting this reactive window through the combination of dual-source NaClO and middle-enthalpy SeO_2, we successfully avoided the kinetic traps of inert oxides and the structural limitations of single-anion salts. This strategy enabled the engineering of a homogeneous, highly conductive, and mechanically robust SE.

4 | Local Coordination Analysis and Dynamic Mechanism

Understanding the structure-activity relationship of SEs in amorphous, disordered state, especially in novel inorganic viscoelastic systems, is crucial for advancing ionic conduction mechanisms. In the Raman spectra of Figure 3a, a broad peak at ~75 cm^{-1} corresponds to Al–Cl stretching and bending vibrations. While standard $AlCl_3$ and $NaAlCl_4$ exhibit distinct peaks near 300 cm^{-1} ($AlCl_6$ octahedra) and 350 cm^{-1} ($AlCl_4^-$ tetrahedra), respectively [28, 29], these features are absent in both NACO and NACDO. This indicates that oxygen incorporation disrupts the symmetry of $AlCl_4^-$ units, likely by bridging isolated tetrahedra into extended networks. This structural role of oxygen is further supported by FTIR spectroscopy (Figure 3b), which reveals characteristic bands corresponding to $AlCl_4^-$ (450–500 cm^{-1}) and Al–O–Al linkages (660–680 cm^{-1}) [30, 31]. In amorphous materials, such bridging oxygen atoms within the Al–O–Al motifs typically function as network formers [16, 32]. Notably, despite the tendency of chlorine to precipitate as crystalline NaCl upon coordination with transition metals, no NaCl reflection are observed in either synchrotron XRD (SXRD) or neutron powder diffraction (NPD) patterns [33] (Figure S13). This absence confirms that precise control of Na content in precursors effectively suppresses NaCl crystallization.

X-ray absorption near-edge structure (XANES) and extended x-ray absorption fine structure (EXAFS) analyses were carried out

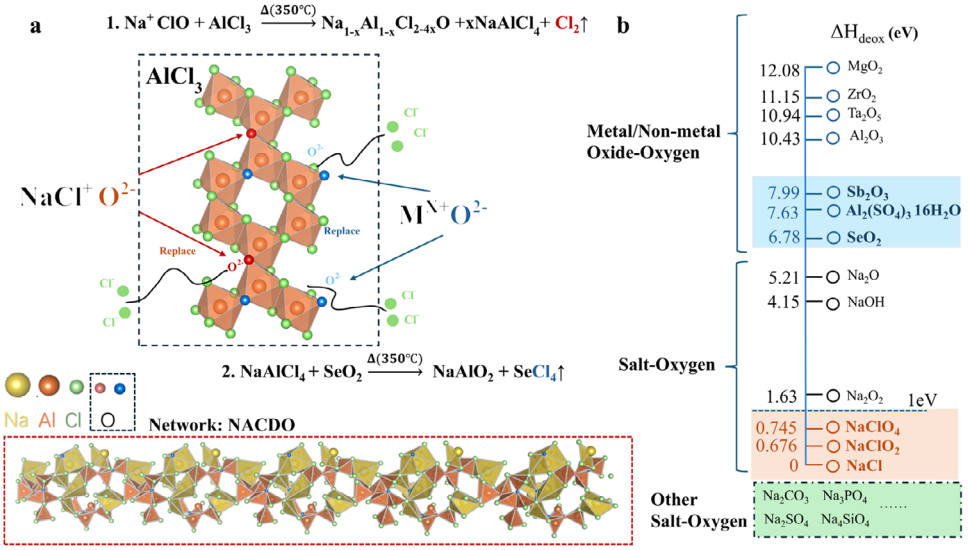

FIGURE 2 | (a) Schematic diagram of the reaction between precursor and $AlCl_3$. The resulting network structure exhibits short-range local ordering derived from computational simulations. (b) Comparison of the ΔH_{deox} values of different oxides. The extra specific calculated values are provided in Tables S3, S4, and S5.

at the K-edges of Al, O and Cl to gain deeper insight into the local structures of NACDO and NACO. XANES confirms that NACO and NACDO retain structural motifs from both $AlCl_3$ and Al_2O_3 [34]. The Al K-edge spectrum overlaps with those of $AlCl_3$ and Al_2O_3 (Figure 3c). The O K-edge spectrum shows a broad peak at 540 eV, characteristic of covalent Al–O–Al bonding in Al_2O_3 (Figure 3d) [32, 35]. Given that the Cl K-edge spectral features of NACDO overlap with those of $AlCl_3$ and NaCl, its content requires further data processing to be distinguished (Figure 3e). Wavelet-transformed EXAFS (Figure 3f) reveals that Cl participates primarily in Al–Cl bonds, with minor Na–Cl contributions. Quantitative EXAFS fitting estimates average chloride coordination numbers of 1.0 around Al and only 0.38 around Na (Tables S6 and S7), indicating fewer Na–Cl bonds than expected and thus a higher concentration of mobile, "free" Na^+ ions. ^{23}Na nuclear magnetic resonance (NMR) spectra corroborate this interpretation: NACDO displays a single sharp resonance at −10.6 ppm, characteristic of a highly disordered Na^+ environment, similar to observations in other amorphous Na–Al–Cl–O systems [4, 26, 36] and disordered chlorides like $NaTaCl_6$ and Na_2S–$ZrCl_4$ [18, 22]. In contrast, NACO exhibits additional minor peaks assignable to residual NaCl (7.2 ppm) and $NaAlCl_4$ (−13 to −18 ppm) (Figure 3g). ^{27}Al NMR further elucidates the structural impact of oxygen incorporation. While crystalline $NaAlCl_4$ shows a peak near 100 ppm ($AlCl_4^-$) [37], oxygen incorporation give rise to signals at 60–90 ppm (short Al–O chains) and 30–40 ppm (extended Al–O chains) [11, 13]. Concurrently, the intensity of the $AlCl_4^-$ resonance decreases significantly while that of the short-chain region increases, independently confirming an increase in bridging oxygen species upon SeO_2 addition. Notably, the weak signal intensity in the 30–40 ppm region for NACDO (Figure 3h) is likely attributable to mechanical disruption of long-chain structures during sample grinding. Furthermore, synchrotron atomic pair distribution function (PDF) analysis reveals shortened Al–O bond lengths (1.3–1.5 Å) in both NACO and NACDO relative to reference Al_2O_3 [11], suggesting a denser local structure that may lower ion migration barriers (Figure 3i).

Time-of-flight secondary ion mass spectrometry (ToF-SIMS) identifies a range of polyanionic clusters in NACO and NACDO, including monomers ($AlOCl_2^-$, $AlCl_4^-$), dimers ($Al_2O_2Cl_3^-$), and trimers ($Al_3O_4Cl_2^-$, $Al_3O_5Cl_3^-$), confirming a viscoelastic network with chain-like connectivity. Notably, prolonged sputtering even reveals longer fragments (e.g., $Al_4O_4Cl_5^-$, $Al_6O_8Cl_3^-$), which exhibit a broader spatial distribution compared to short- and medium-chain species under identical conditions (Figure 4a,b). A 3D rendering of the internal structure corroborates the mass spectral data and confirms the presence of an extended network-like architecture (Figure 4c–f). It should be noted that ToF-SIMS signal intensities do not directly reflect absolute concentrations. Signals from the immediate surface can be influenced by matrix effects, variations in ionization efficiency, and altered fragmentation patterns. In contrast, deeper structural information, more representative of the bulk, is better accessed from the subsurface region.

To gain deeper insight into the influence of structure on dynamic mechanisms, we employed ab initio molecular dynamics (AIMD) simulations to compare crystalline and amorphous structures. The pristine $NaAlCl_4$ crystallizes in the orthorhombic system, where sodium ions form seven-coordinate polyhedra with chlorine. These polyhedra connect to $AlCl_4^-$ tetrahedra via edge-sharing or corner-sharing configurations (Figure 5a, left). This specific crystalline arrangement lacks efficient and fast Na^+ diffusion channels when compared to systems like NASICON and Na_3PS_4 [3]. In contrast, the introduction of oxygen disrupts these crystalline constraints, inducing a high degree of disorder throughout the NACDO system (Figure 5a, right). Specifically, the vertices of $AlCl_4^-$ tetrahedra are randomly substituted by 1 to 3 oxygen atoms, allowing the tetrahedra to connect with more chloroaluminate units and form an extended network. Besides, chlorine atoms at the vertices of the sodium-chlorine polyhedra are replaced, resulting in oxygen-terminated vertices. These modified polyhedra then form face-sharing and edge-sharing connections with the chloroaluminate tetrahedra, actively participating

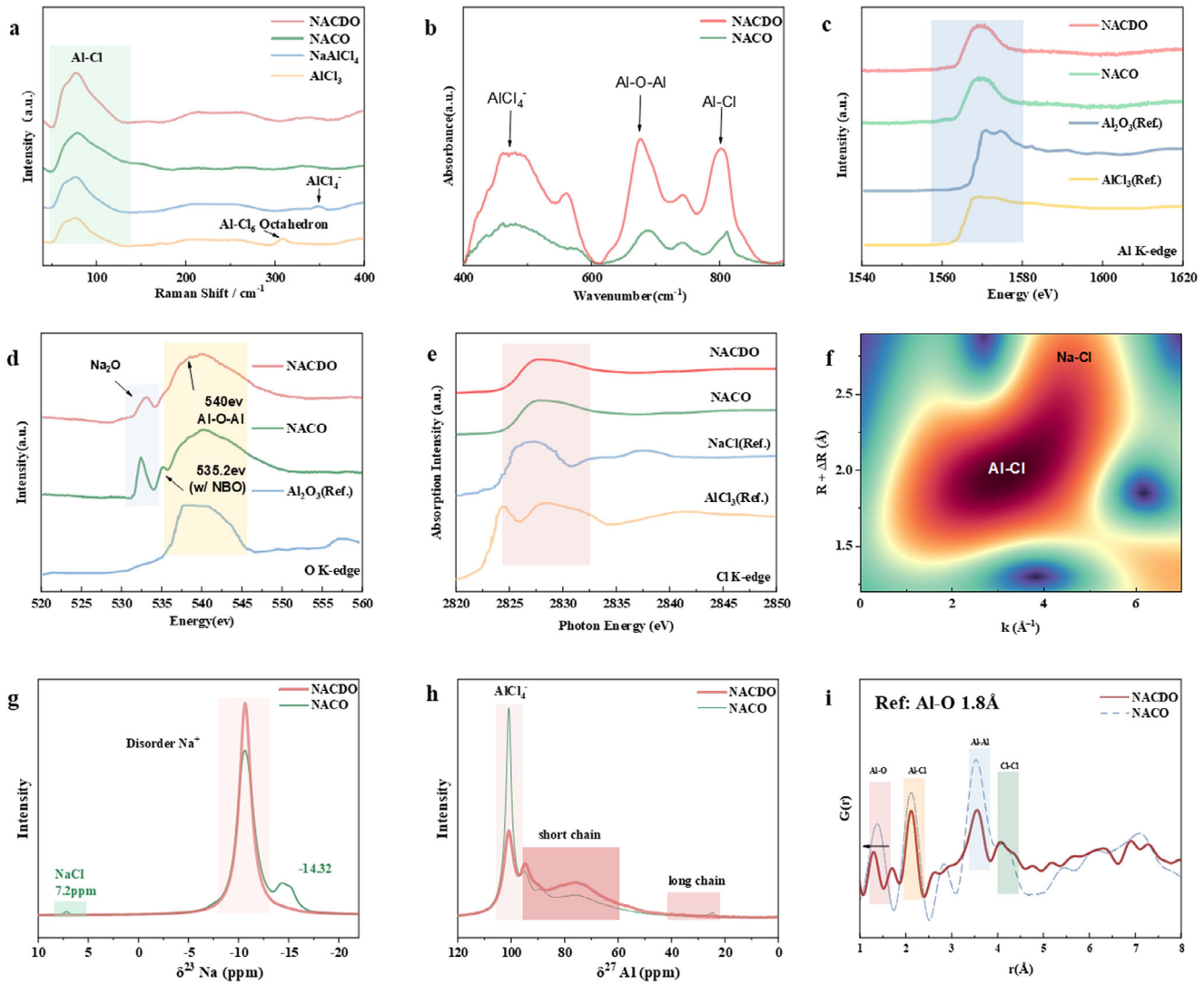

FIGURE 3 | (a) Raman spectra of Al-based SEs and crystalline $NaAlCl_4$, $AlCl_3$ references. (b) FTIR spectrum of NACO and NACDO. (c, d) XANES of NACO and NACDO at Al- and O K-edge, respectively. (c) Al K-edge, Ref of $AlCl_3$ and Al_2O_3 [11]. (d) O K-edge, Ref of Al_2O_3 [38]. (e) EXAFS of NACO and NACDO at Cl K-edge. Ref of $AlCl_3$ and NaCl [39, 40]. (f) Wavelet-transformed EXAFS contour plots of NACDO at Cl K-edge. $R + \Delta R$ represents the radial distance, and ΔR indicates the distance correction due to phase shifts. The original EXAFS signal $\chi(k)$ is weighted by k^2, and k represents wavenumber. (g) ^{23}Na NMR and (h) ^{27}Al NMR of NACO and NACDO. (i) Synchrotron PDF measurement of NACO and NACDO electrolytes.

in the network construction. When viewed beyond a single unit cell, this results in a 3D interconnected disordered arrangement. Unlike conventional rigid amorphous SEs, the room-temperature viscoelasticity of the NACDO-based electrolyte indicates that its segmental structure possesses inherent mobility [9, 31, 40].

These structural differences lead to distinct migration trajectories for Na, Al, and O atoms, as revealed by the simulations. In the rigid crystal framework, Na, Al, and Cl atoms are confined to their lattice sites. As shown in the Mean Square Displacement (MSD) analysis (Figure 5d), these ions merely vibrate around fixed positions or undergo displacement within an extremely small range. Within 20 ps, Cl atoms barely move, while Na and Al atoms return to their original positions after minimal displacement, maintaining structural stability and preventing collapse (Figures 5b and S14). Conversely, the NACDO system, which features a segmental/network structure, exhibits significant atomic mobility. Atoms exhibit greater randomness and dispersity in their migration, distributing themselves around the segment arms (Figures 5c and S14). Notably, Al and Cl do not act solely as static framework ions; their movement confirms the phenomenon of segmental motion. MSD simulations confirm that elements other than Na^+ specifically O, Al, and Cl—undergo displacement. Since the structure is primarily composed of an aluminum-oxygen-chlorine (Al-O-Cl) framework, the displacement patterns of these elements vary consistent with the overall movement of structural segments. Over a 60 ps simulation, the MSD of Al and O atoms converge, indicating the uniformity of the segmental motion within the main Al-O-Al chains (Figure 5e). Furthermore, the radial distribution function (RDF) calculations in Figure S14 show that the Al-O-Al linkages yield an Al-Al distance (2.63/3.31 Å) shorter than twice the Al-O length (1.79 Å). Additionally, the introduction of oxygen also shortens the Na-Al distance, which may help decrease the migration distance for ions. The same phenomena were observed in the MSD and atom distribution diagrams for Ta- and In-based SEs (Figure S15).

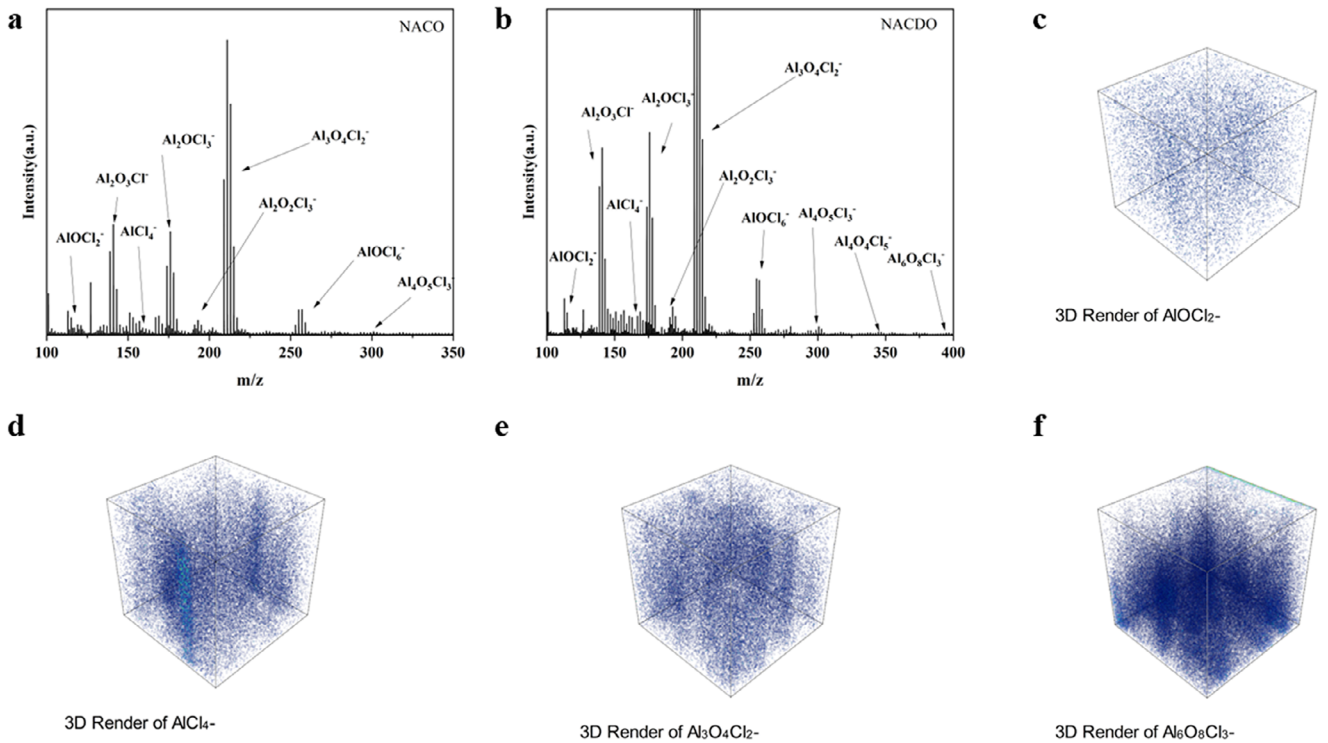

FIGURE 4 | Negative-ion TOF-SIMS characterization. (a) Mass spectrum of NACO. (b) Mass spectrum of NACDO. (c–f) 3D Render of anion-radicals in NACDO. (c) $AlOCl_2^-$, (d) $AlCl_4^-$, (e) $Al_3O_4Cl_2^-$, (f) $Al_6O_8Cl_3^-$.

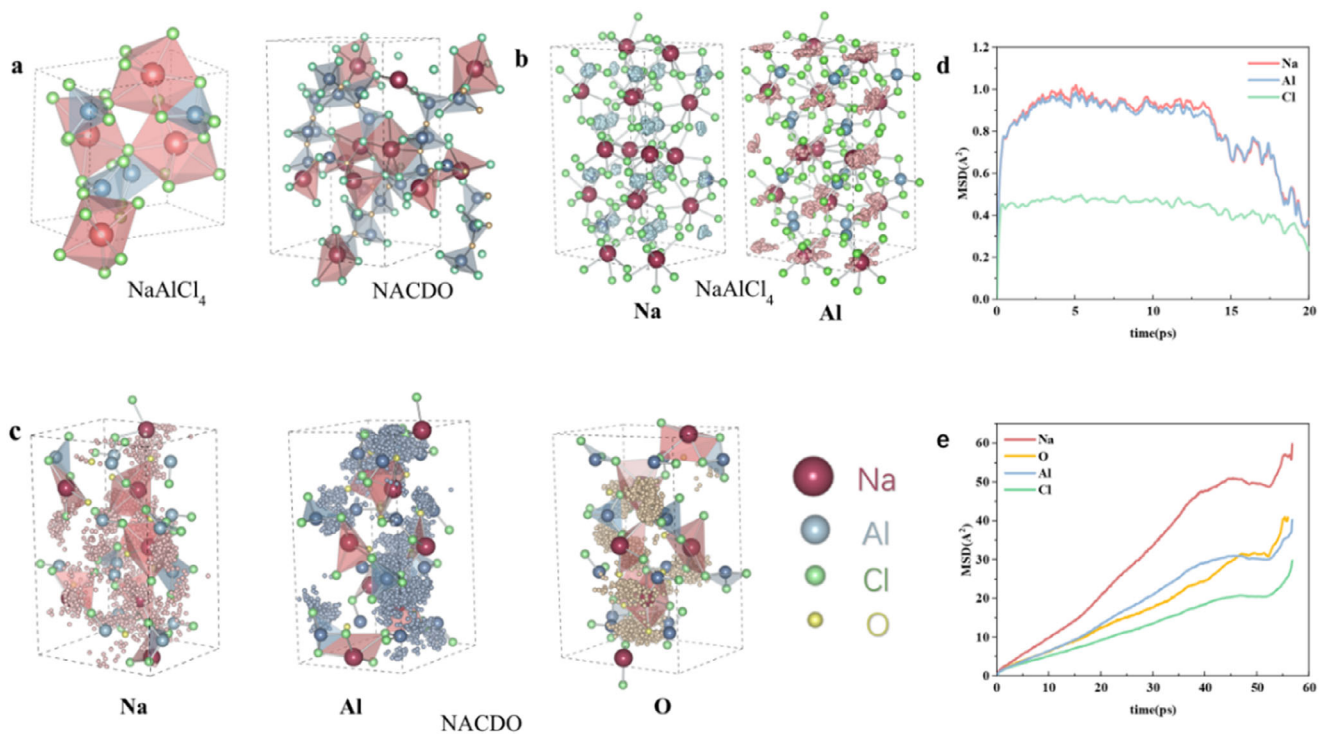

FIGURE 5 | (a) Structure of $NaAlCl_4$ (NAC) and NACDO by AIMD simulation. (b) Corresponds to Na and Al atom position distribution in the $NaAlCl_4$, respectively. (c) Corresponds to Na, Al, and O atom position distribution in the NACDO, respectively. To illustrate the migration behaviors of the viscoelastic amorphous SE and the crystalline SE, polyhedral models and ball-and-stick models were used more intuitively. (d, e) MSD of various atoms at 600 K. (d) MSD of $NaAlCl_4$. (e) MSD of NACDO.

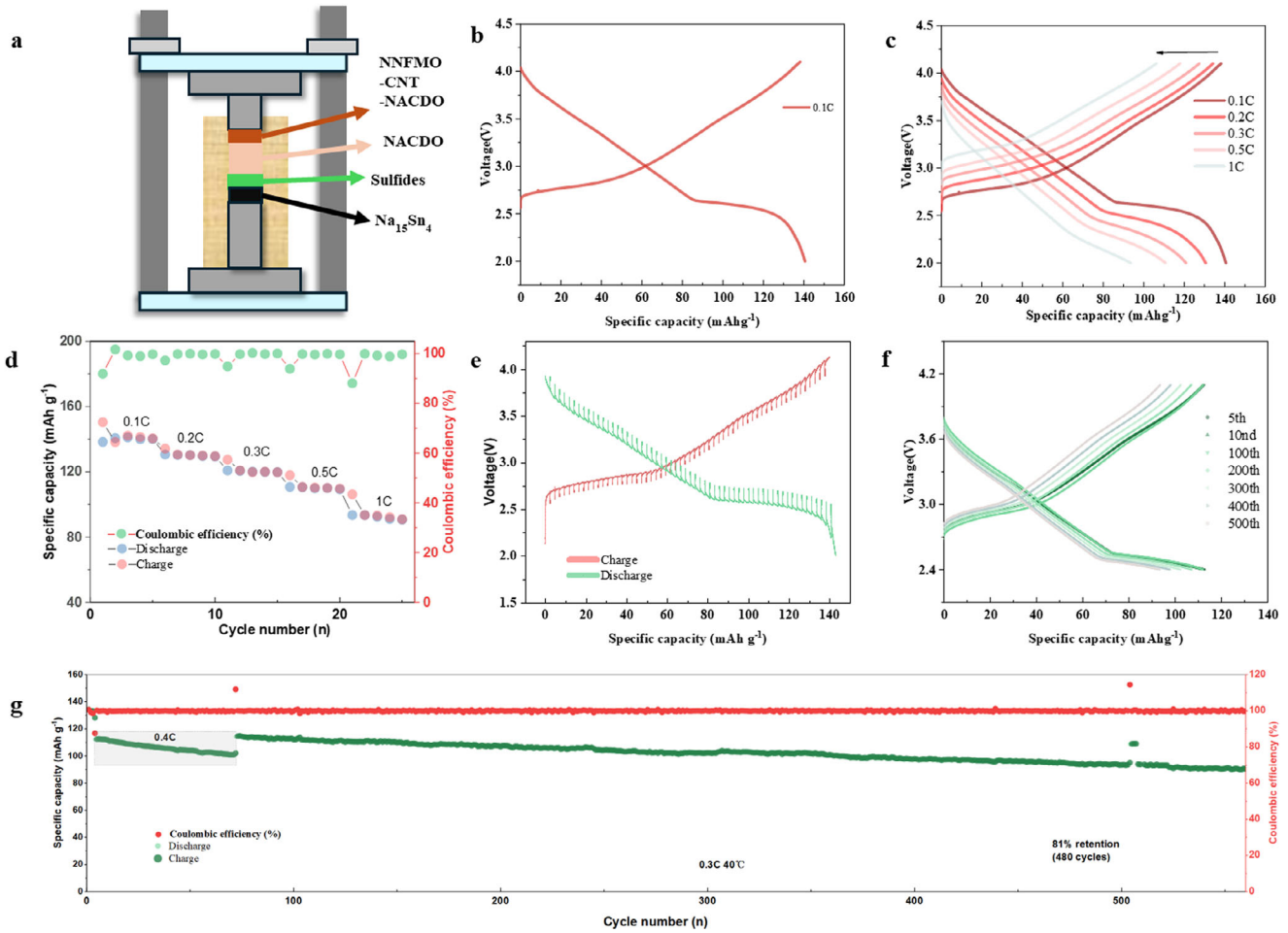

FIGURE 6 | (a) Schematic diagram of ASSNaB assembly. CNTs, carbon nanotubes. (b) First-cycle 0.1C charge-discharge of SSB (1C = 140 mAh g^{-1}, 30°C, 2–4.1 V). (c,d) Charge-discharge curves, and rate performance of SSB at different current densities, 2–4.1 V. (e) GITT curves of SSB in the first cycle, 30°C. (f,g) Charge-discharge curves and cycling performance of SSB at 0.3 C, 40°C, 2.4–4.15 V. Areal loading: 5.2 mg/cm^2.

5 | The Performance of NACDO-Based ASSNaB and Compatibility With Cathode

To evaluate the electrochemical performance of the novel viscoelastic SE (NACDO), a sandwich-type all-solid-state Na battery (ASSNaB) was assembled (Figure 6a) using the layered oxide cathode $NaNi_{0.4}Fe_{0.2}Mn_{0.4}O_2$ (NFM424), selected for its suitable voltage window and high capacity [41] (Figure S16). NACDO-based ASSNaB exhibits superior performance, delivering an initial discharge capacity of 140.6 mAh g^{-1} at 0.1C, approaching that of liquid-electrolyte batteries (Figure 6b) [42]. Cyclic voltammetry reveals excellent reversibility between NACDO and NFM424: after minor fluctuations due to SEI formation in the first cycle, the subsequent three cycles show nearly overlapping profiles (Figure S17). Rate capability tests further confirm robust kinetics, with reversible capacities of 140.5, 130.5, 120.8, 110.5, and 93.3 mAh g^{-1} achieved at 0.1 C, 0.2 C, 0.3 C, 0.5 C, and 1 C, respectively (Figure 6c,d). Galvanostatic intermittent titration technique (GITT) analysis shows low polarization and fast Na^+ transport within the cathode. The Na^+ diffusion coefficients (D_{Na^+}) derived from GITT data range from 10^{-11} to 10^{-8} cm^2 s^{-1} during both charge and discharge processes, indicating favorable Na^+ transport kinetics. These high diffusivity values are consistent with the minimal overpotential observed in the GITT profiles (Figure 6e, Figure S18). In contrast, batteries using the sulfide electrolyte Na_3PS_4 suffer from low ionic conductivity (Figure S19), leading to rising charge plateaus, underdeveloped discharge plateaus at higher currents, and incomplete active material utilization. Linear sweep voltammetry (LSV) indicates NACDO begins decomposing at ~2.2 V (Figure S20); thus, the cycling voltage window was set to 2.4–4.15 V to ensure stability. Long-term cycling was performed as follows: initial activation at 0.1C, followed by dozens of cycles at 0.4C, then continued cycling at 0.3C (Figure 6f, g). At 40°C and 0.3C over 480 cycles, the cell retained > 80% capacity with an average Coulombic efficiency of 99.91%, highlighting good interfacial stability between the Al-based SE and both the cathode and sulfide components. Regarding long-term cycling, the NACDO | Oxide cathode battery retains approximately 50% of its initial capacity after 1200 cycles, demonstrating reasonable durability despite gradual degradation over extended operation. These metrics surpass those of other Al-based SEs paired with sodium layered oxide cathodes (Table S8). However, NACO prepared solely with NaClO as the oxygen source exhibits mediocre electrochemical performance and low initial Coulombic efficiency. This underscores the effectiveness of the dual oxygen source strategy (Figure S21).

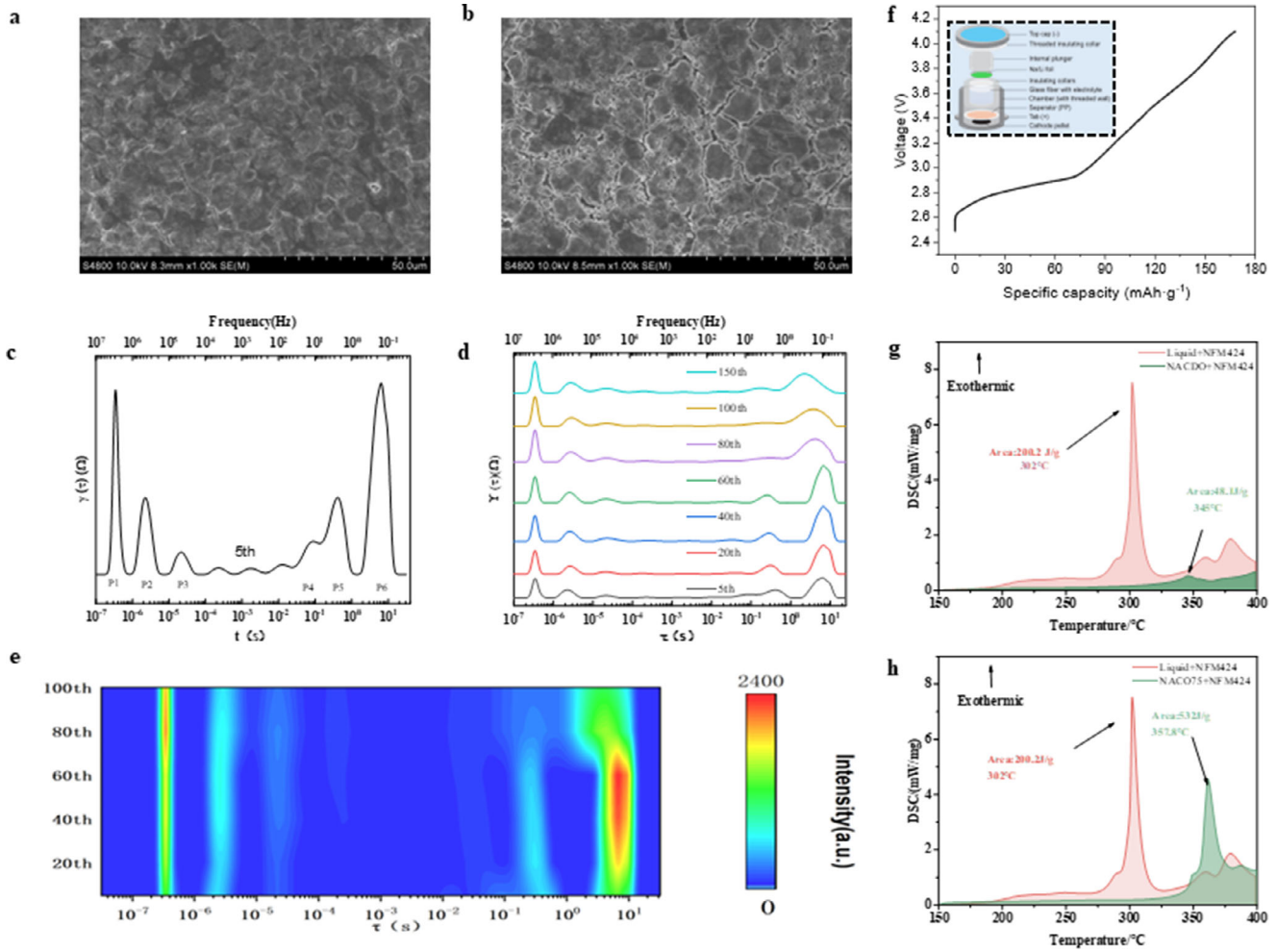

FIGURE 7 | SEM images of NACDO-based composite cathode. (a) before cycling. (b) after cycling. (c–e) In situ DRTS calculated from EIS measurements. The τ represents relaxation time, and $\gamma(\tau)$ stands for distribution function of relaxation times. (c) fifth cycle. (d) different cycles. (e) DRT 2D intensity color map of distribution of relaxation times curves abstracted from (c). (f–h) Thermal stability test of electrolytes with charged cathode powder. (f) charged to 4.1 V NFM424 cathode. The inset shows the coin-cell assembly of the charged cathode [27]. (g) NACDO electrolyte with NFM424 cathode. (h) NACO75 electrolyte with NFM424 cathode.

Good interfacial compatibility governed by both electrochemical and mechanical factors is critical for achieving high capacity and long-term cycling stability in solid-state batteries. SEM reveals that the composite cathode exhibits more pronounced gaps and cracks after cycling compared to its pristine state (Figure 7a). However, thanks to the low melting point of NACDO and the deformability of the cathode particles, intimate contact between the electrolyte and cathode particles, achieved through melt-processing and cold pressing, is largely preserved even after cycling (Figure 7b). This physical stability is complemented by strong chemical compatibility, as confirmed by x-ray photoelectron spectroscopy (XPS). Minimal shifts in the Al 2p and Cl 2p peaks after the third cycle (Figure S22) correlate with the stabilization of the SEI, consistent with cyclic voltammetry results.

To further probe interfacial evolution during extended cycling, in-situ electrochemical impedance spectroscopy (EIS) was coupled with distribution of relaxation times (DRT) analysis. The DRT [43] spectrum shows six characteristic peaks (Figure 7c): P1 ($<10^{-6}$ s) corresponds to contact resistance among cathode particles, carbon nanotubes, and the current collector. Its intensity increases up to the 80th cycle, likely due to mild current collector corrosion. P1 does not strictly stabilize after 80 cycles; rather, it exhibits a non-monotonic evolution: a pronounced increase during cycles 5–80, followed by a slight decrease and then a gradual, limited increase up to cycle 150. This variation beyond 80 cycles is minor compared to the initial rise. (Figure S23). P2/P3 (10^{-6}–10^{-4} s) reflect Na^+ transport across the Na_3PS_4 and halide electrolyte layers, respectively [44]. Their slow shift to lower frequencies and increasing magnitude suggest SEI growth, which lengthens ion migration paths. P4/P5 (10^{-2}–1 s) relate to charge transfer at the anode– and cathode–electrolyte interfaces. Their stability throughout cycling indicates the formation of a robust, passivating interphase that supports durable performance. P6 (>1 s), associated with solid-state Na^+ diffusion within cathode particles, initially intensifies and then gradually declines [45] (Figure 7d,e), possibly due to irreversible Na^+ deintercalation or vacancy formation that enhances local ionic flux [45].

Thermal stability was assessed by mixing charged NFM424 (Figure 7f) with electrolytes and analyzing exothermic behavior via differential scanning calorimetry (DSC). NACDO significantly suppresses thermal reactivity: the onset of exothermic reactions is delayed by ~40°C relative to conventional liquid electrolytes, and the total heat release is reduced by 75% or more. Crucially, no exothermic peak is observed below 300°C, the typical thermal runaway threshold for organic electrolyte/layered oxide systems, highlighting enhanced safety [46, 47].In comparison, the benchmark viscoelastic electrolyte NACO75 [9] also improves thermal stability (onset delayed by ~50°C and 30% less heat vs. liquid), but NACDO demonstrates markedly superior performance (Figure 7g,h). Nevertheless, component-level thermal stability at the cathode-electrolyte interface does not guarantee system-level safety, as multiple additional influencing factors must be considered and warrant further investigation. Collectively, these results confirm that NACDO establishes a mechanically resilient, electrochemically stable, and thermally safe interface with high-voltage layered oxide cathodes, key attributes for practical ASSNaBs.

6 | Conclusion

In summary, we present a rational design strategy for viscoelastic SEs that classified oxygen-containing compounds into two functional categories: "Salt-Oxygen" and "Metal/Non-metal Oxide-Oxygen." These components synergistically enable $AlCl_3$ to form a stable, room-temperature viscoelastic network. By integrating experimental screening with thermodynamic calculations of deoxygenation enthalpy (ΔH_{deox}), we efficiently identify optimal precursors and developed NACDO—an $AlCl_3$-based SE that simultaneously achieves viscoelasticity, high room-temperature ionic conductivity, and optical transparency. Structurally, NACDO's highly disordered framework facilitates rapid Na^+ transport, while polymer-like segmental dynamics confirmed by computational analysis underpin its mechanical adaptability. When paired with an uncoated, high-capacity layered oxide cathode (NFM424), NACDO delivers exceptional cycling stability. Its low melting temperature enables effective infiltration into composite cathodes at mild processing conditions, ensuring intimate interfacial contact. Furthermore, NACDO exhibits outstanding thermal compatibility with oxide cathodes, significantly suppressing exothermic reactions and mitigating thermal runaway risks. This multi-oxygen-source design paradigm offers a generalizable approach for developing advanced SEs, providing a promising pathway toward safe, high-performance ASSNaBs.

7 | Experimental Methods

7.1 | Material Synthesis

All preparations and sample treatments were carried out under an Ar atmosphere ($O_2 < 1$ ppm, $H_2O < 1$ ppm). $AlCl_3$ (Macklin, 98%), $InBr_3$ (Adamas, 99.9%metals basis), $TaCl_5$ (Adamas, 99.9%metals basis), SeO_2 (Innochem, 99%), NaClO (Macklin, effective chlorine ≥ 30%), $NaClO_2$ (Innochem, 80%), $NaClO_4$ (Alfa, 99.9%), and Sb_2O_3 (Macklin ≥ 99.9%) were used as the starting materials without further purification. The selection of 98% purity $AlCl_3$ was primarily driven by cost-effectiveness and industrial scalability, as high-purity (≥ 99.9%) halide precursors are significantly more expensive (often several-fold higher), which would hinder large-scale application. For preparing raw materials, a ~1 g stoichiometric mixture of metal halide ($AlCl_3$, $InBr_3$, or $TaCl_5$), oxides (Sb_2O_3 or SeO_2), and NaClO was placed in the mortar and hand ground for 3 min. Next, put the raw materials into ceramic crucible, using a muffle furnace to low-temperature melt at 300°C–400°C for 0.5 h (the heating rate is 10°C/min). Then quench the resulting liquid to room temperature. When the obtained liquid Al-based electrolyte is slightly cooled, pour it onto a specially made flat plate, then use a special rolling rod to spread the liquid into a film. The other obtained SEs (Ta, In) were hand-ground with agate and pestle in the Ar-filled glovebox to get target powder samples for future use.

Na_3PS_4 was synthesized by a mechanochemical technique using a high-energy ball mill machine. The starting materials of Na_2S (Adamas, 99.9%) and P_2S_5 (Sigma Aldrich, 99%) were milled at 500 rpm for 10 h in a 50 mL ZrO_2 ball mill jar. The ball-milled product was extracted from the jars in the glove box, pelletized at 3 T, and then loaded into vacuumed quartz tubes. The Na_3PS_4 was obtained after being annealed at 270°C for 2 h with a heating rate of 5°C/min. The obtained Na_3PS_4 was extracted from the quartz tubes and manually ground into powder for future use.

$NaNi_{0.4}Fe_{0.2}Mn_{0.4}O_2$ was synthesized by a routine high-temperature solid-state method. Stoichiometric amounts of Na_2CO_3 (Alfa, 99.5%), NiO (Aladdin, 99.9%), Fe_2O_3 (Aladdin, 99.9%), and MnO_2 (Aladdin, 98%) were mixed thoroughly in an agate mortar. Subsequently both precursors were calcined at 950°C for 15 h in air. Finally, the samples were cooled to 100°C naturally in the muffle furnace and transferred into an Ar-filled glovebox immediately.

7.2 | Characterizations

Powder XRD measurements were conducted at room temperature on a Bruker D8 diffractometer equipped with Cu-Kα (λ = 1.5406 Å) radiation. Regular tests were conducted at a scan rate of 10° min^{-1} from 10° to 80°. Before the test, it is necessary to first seal the XRD sample slide with plastic wrap and vacuum grease in a glove box to isolate it from air. X-ray absorption near-edge structure (XANES) of Al K-edge and O K-edge XAS data were collected on the BLO2BO2 beamline at the Shanghai Synchrotron, part of Shanghai Advanced Research Institute, Chinese Academy of Sciences. Cl K-edge x-ray absorption fine structure (XAFS) data on the MEX1 beamline at the Australian Synchrotron, part of Australia's Nuclear Science and Technology Organization (ANSTO). All XAS data were analyzed with the Athena software, and the EXAFS data were processed with the Artemis program. Synchrotron PDF and Synchrotron XRD data were collected on the ID07-Engineering Materials Beamline of High Energy Photon Source (https://cstr.cn/31138.02.HEPS.ID07). SEM images and element mapping were obtained by using a Hitachi S-4800 field-emission SEM equipped with energy dispersive spectroscopy (EDS). Before the SEM test, the sample also needs to be sealed in advance inside a glove box using a vacuum transfer stage to isolate it from air and protect the sample. The Raman spectra were collected on a HORIBA Scientific LabRAM HR Evolution. Raman spectrometer equipped with a

532.03 nm laser. The XPS data were collected with XPS spectra and were probed by using an ESCALAB 250 Xi (Thermo Fisher). All samples were placed into air-tight holders to avoid possible air exposure during XRD and Raman characterizations. The Fourier transform-infrared (FTIR) spectroscopy was collected by Bruker VERTEX 70 V. A vacuuming process is required during the test. The thermal behavior of the electrolyte was examined using DSC on NETASCH DSC 300 Caliris. The sample was loaded in the aluminum pan and hermetically crimp-sealed inside the Ar-filled glove box. The DSC measurements were carried out at a heating rate of 10°C min^{-1} from −150°C to 300°C. Thermal stability tests were also performed by a DSC300 Classic (NETZSCH) instrument. All the preparation steps were performed in an argon filled glove box. The heating rate was 5°C per min. The instrument had been calibrated, and the Proteus software was used for data analysis, in 50°C–450°C range. The $NaNi_{0.4}Fe_{0.2}Mn_{0.4}O_2$ cathode material was collected from a specially designed half battery. The $NaNi_{0.4}Fe_{0.2}Mn_{0.4}O_2$ cathode material were mixed with VGCF at an 85:15 ratio, then pressed into a disk with a diameter of 15 mm. The cathode disk and metal Na was assembled to a half battery, using polypropylene and glass fiber (Whatman GF/D) as the separator. The electrolyte was a solution of 1 mol•L^{-1} $NaPF_6$ in ethylene (EC), diethyl carbonate (DEC) (1:1 in volume), purchased from DoDoChem. After charging, the battery was constant voltage charged at the ending voltage for 30 min, to mitigate the inhomogeneity during charging. Then the battery was disassembled to collect the charged cathode material. The collected cathode material was washed by dimethyl carbonate (DMC, Sigma-Aldrich) three times, to minimize the implication of cathode electrolyte interface. After washing, the charged cathode material was vacuum dried.

The stress-strain curves were measured using a dynamic mechanical analyzer (DMA, TA850) at room temperature. For the micropillar compression tests, ion beam processing was first employed to fabricate micropillars on the material surface. The as prepared micropillars were then compressed under a 10 μm indenter. ToF-SIMS analysis was performed in negative ion mode using an IONTOF TOF.SIMS 5 instrument. NMR measurements were performed on a Bruker AVANCE III HD 600 WB spectrometer. MAS Spinning rate:12 kHz.

7.3 | Conductivity Measurements

The ionic conductivity of SEs was measured by EIS. Typically, for powder sample, 100 mg of the powder sample was pressed into pellets (diameter 10 mm) at 400 MPa in the Ar-filled glovebox. For the Al-based thin film sample, cut it into a 10 mm (piece), then place it into a mold and tighten it with nuts to proceed with the test. EIS experiments were performed within a frequency range of 1 MHz to 100 Hz at temperatures ranging from −15°C to 75°C using a CHI760F potentiostat/galvanostat (Ch instruments). The EIS measurements were recorded at different temperatures, and data was collected after the sample was held at the target temperature for over 60 min to allow for equilibration. The activation energy (E_a) was calculated from the slope of the resulting Arrhenius plot. The electronic conductivity of the sample was measured according to the direct current (DC) polarization measurement on cold-pressed pellets with applied voltages from 0.2 to 1 V at room temperature. The activation energies of the as-prepared SEs were calculated using the following equation:

$$\sigma T = \sigma_o \exp(-E_a/k_B T) \quad (1)$$

where σ is the ionic conductivity, σ_0 is the Arrhenius prefactor, T is absolute temperature, E_a is the activation energy and k_B is the Boltzmann constant. Galvanostatic charge–discharge performance tests were performed with a Land CT3001A battery test system.

7.4 | Electrochemical Characterizations

ASSNaBs were assembled by using NACDO as the electrolyte, NFM424 as the cathode active material, Na_3PS_4 as the interlayer, and $Na_{15}Sn_4$ (~0.1 V vs. Na/Na^+) as the anode. First, weigh NFM424, NACDO, and CNT according to a mass ratio of 70:25:3, then place them on a small heating stage and heat to 150°C for uniform mixing. Next, add the mixture and 2 mg of PTFE into a mortar, fully pound for 20 min until uniformly dispersed. Then, following the method for dry-process electrodes, uniformly roll manually for 20–30 min to obtain the cathode sheet. The battery is fabricated through mechanical pressing in the Ar-filled glovebox. Briefly, 50 mg Na_3PS_4 was compressed at ~100 MPa to form a SE layer. The prepared NACDO can be formed into a 9 mm film using a 9 mm punching cylinder. And put this film on one side of the Na_3PS_4 pellet layer, and further pressed at ~100 MPa, and 3 mg NFM424 cathode composite were put on one side of the NACDO film and further pressed at ~400 MPa. Finally, 50 mg $Na_{15}Sn_4$ alloy (~0.1 V vs Na+/Na) is pressed on the Na_3PS_4 side at ~350 MPa. The cells were cycled under external pressure which is applied by tightening the nut on the external steel post. Accordingly, an external stacking pressure of 10-15 MPa was adopted throughout the cycling tests in this work. This pressure range was selected as it is sufficient to ensure stable interfacial contact while being substantially lower than the pressures often required for oxide or sulfide-based solid-state batteries (which frequently exceed 50–100 MPa). And the galvanostatic charge-discharge measurement was conducted on a battery testing system (CT-3001A) in the potential range of 2–4.15 V versus Na/Na^+. The electrochemical stability of NACDO SE was evaluated by LSV measurements using versatile CHI760F potentiostat/galvanostat (CH instruments). with a $Na_{15}Sn_4|Na_3PS_4|$ SE |SE + C (weight ratio: NACDO:C = 8:2) cell at 0.1 mV S^{-1}. The cell assembly procedure is like that of the ASSNaBs, while module cells were used without external pressure applied during cycling. All the batteries were assembled in the Ar-filled glovebox and then preceded by a rest period of 2 h for equilibrium before electrochemical measurement.

7.5 | Computational Method

In this work, all non-crystalline structures were constructed from the $NaAlCl_4$, $NaInBr_4$, $NaTaCl_6$ framework, respectively. (from Materials Project No. mp-23363) via elemental substitution and generated using ab initio molecular dynamics (AIMD) simulations based on a heat-and-quench protocol [9, 48]. All AIMD simulations were performed with the VASP package, employing DFT [49], at the generalized gradient approximation (GGA) level with the PBEsol exchange–correlation functional [50, 51]. The

simulations were carried out in the canonical ensemble (constant number of atoms, volume, and temperature) with a time step of 0.5 fs. Each system was heated to 900 K and maintained for 30 ps to achieve melting, followed by equilibration at 600 K for an additional 30 ps to obtain a physically reasonable amorphous configuration. During equilibration, the first 10 ps were used for structural stabilization, while the subsequent 20 ps were used for statistical analysis of structural information and ion-migration behavior, including the RDF, the mean square displacement (MSD), and the migration trajectories of Na^+ ions. DFT calculations were performed by Vienna ab initio Simulation Package [51] (VASP 5.4.4) using the Perdew-Burke-Ernzerhof (PBE) [52] functional within GGA. A homogeneous Monkhorst-Pack k-point grid was set to ensure that the k-point intervals in reciprocal space did not exceed 0.05 $Å^{-1}$. A kinetic energy cutoff of 520 eV was used for plane-wave basis set. The convergence criteria for total free energy and forces were set as 1.0×10^{-5} and 0.01 eV $Å^{-1}$, respectively.

Author Contributions

Lihao Tang: Writing – original draft, Writing – review and editing, investigation, validation, data curation. **Liwei Jiang**: Calculation. **Yang Huang**: Calculation. **Rui Bai**: validation. **Jingchen Lian**: Calculation. **Haibo Wang**: validation. **Hao Jiang**: validation. **Bowen Wang**: validation. **Xubin Wang**: validation. **Yuyao Wang**: validation. **Jian Peng**: resources. **Fei Xie**: supervision. **Xiaohui Rong**: supervision. **Liquan Chen**: supervision, funding acquisition. **Yong-Sheng Hu**: resources, funding acquisition. **Yaxiang Lu**: writing – original draft, writing – review and editing, resources, project administration, supervision, funding acquisition.

Acknowledgements

This work was supported by the Beijing Natural Science Foundation (JQ25009), Commanding Heights of Science and Technology of Chinese Academy of Sciences (LDES15 0000), and the National Natural Science Foundation (NSFC) of China (52394170-52394174, 52521001, 22579169).

Conflicts of Interest

The authors declare no conflicts of interest.

Data Availability Statement

The data that support the findings of this study are available from the corresponding author upon reasonable request.

References

1. J. Janek and W. G. Zeier, "Challenges in Speeding up Solid-state Battery Development," *Nature Energy* 8, no. 3 (2023): 230–240.

2. C. Wang, J. Liang, J. T. Kim, and X. Sun, "Prospects of Halide-Based All-Solid-State Batteries: From Material Design to Practical Application," *Science Advances* 8, no. 36 (2022): adc9516.

3. S. Wang, J. Fu, Y. Liu, et al., "Design Principles for Sodium Superionic Conductors," *Nature Communications* 14, no. 1 (2023): 7615.

4. J. Park, J. P. Son, W. Ko, et al., "$NaAlCl_4$: New Halide Solid Electrolyte for 3 V Stable Cost-Effective All-Solid-State Na-Ion Batteries," *ACS Energy Letters* 7, no. 10 (2022): 3293–3301.

5. H. Kwak, J. Lyoo, J. Park, et al., "Na_2ZrCl_6 enabling Highly Stable 3 V All-Solid-State Na-Ion Batteries," *Energy Storage Materials* 37 (2021): 47–54.

6. J. Qu, H. Wu, X. Wang, et al., "Advances in Non/Low-Crystalline Solid-State Electrolytes Enabled by Halide-Based Electrolytes," *Joule* 10, no. 2 (2026): 102260.

7. Y. Tan, J. Gatts, C. Fu, et al., "Dual-Anion Sodium Halide-Based Solid Electrolytes with High Ionic Conductivity and High-Voltage Stability," *Small* 21, no. 29 (2025): 2504677.

8. P. Ridley, L. H. B. Nguyen, E. Sebti, et al., "Amorphous and Nanocrystalline Halide Solid Electrolytes With Enhanced Sodium-Ion Conductivity," *Matter* 7, no. 2 (2024): 485–499.

9. T. Dai, S. Wu, Y. Lu, et al., "Inorganic Glass Electrolytes With Polymer-Like Viscoelasticity," *Nature Energy* 8, no. 11 (2023): 1221–1228.

10. H. Duan, C. Wang, X.-S. Zhang, et al., "Amorphous AlOCl Compounds Enabling Nanocrystalline LiCl With Abnormally High Ionic Conductivity," *Journal of the American Chemical Society* 146, no. 43 (2024): 29335–29343.

11. G. Wang, S. Zhang, H. Wu, et al., "Oxychloride Polyanion Clustered Solid-State Electrolytes via Hydrate-Assisted Synthesis for All-Solid-State Batteries," *Advanced Materials* 37, no. 4 (2025): 2410402.

12. X. Wang, S. Zhang, J. Yue, et al., "A New Class of Carbonate–oxychloride Solid Electrolytes for High-Performance Sodium-Ion All-Solid-State Batteries," *Energy & Environmental Science* 18, no. 22 (2025): 9927–9938.

13. S. Zhang, Y. Xu, H. Wu, et al., "A Universal Self-Propagating Synthesis of Aluminum-Based Oxyhalide Solid-State Electrolytes," *Angewandte Chemie International Edition* 63, no. 27 (2024): 202401373.

14. J. Park, D. Han, J. P. Son, et al., "Extending the Electrochemical Window of Na^+ Halide Nanocomposite Solid Electrolytes for 5 V-Class All-Solid-State Na-Ion Batteries," *ACS Energy Letters* 9, no. 5 (2024): 2222–2230.

15. C. Boo and J. Jang, "Halide and Oxyhalide Solid-State Electrolytes: From Structural Chemistry to Electrochemical Applications in All-Solid-State Na-Ion Batteries," *Materials Today Chem* 54 (2026): 103620.

16. X. Lin, Y. Zhao, C. Wang, et al., "A Dual Anion Chemistry-Based Superionic Glass Enabling Long-Cycling All-Solid-State Sodium-Ion Batteries," *Angewandte Chemie International Edition* 63, no. 2 (2024): 202314181.

17. Z. Huang, N. Yadav, S. Itakura, et al., "Oxygen-Mediated Structural Modulation and Ion Transport in xNa_2O-$TaCl_5$ Glass Electrolytes," *Journal of the American Chemical Society* 147, no. 47 (2025): 43391–43399.

18. Y. Hu, J. Fu, J. Xu, et al., "Superionic Amorphous $NaTaCl_6$ Halide Electrolyte for Highly Reversible All-Solid-State Na-Ion Batteries," *Matter* 7, no. 3 (2024): 1018–1034.

19. T. Zhao, B. Samanta, X. M. de Irujo-Labalde, et al., "Sodium Metal Oxyhalides $NaMOCl_4$ (M = Nb, Ta) With High Ionic Conductivities," *ACS Materials Letters* 6, no. 8 (2024): 3683–3689.

20. J. Leifeld, A. C. Parsons, A. Morscher, et al., "Disorder-Driven Fast Na^+ Transport: From Crystalline to Amorphous Networks in the Mixed-Anion $NaTaO_xCl_{6-2x}$ Oxychlorides," *Advanced Energy Materials* 16, no. 24: 70977.

21. L. Zhou, S. Zhang, W. Li, et al., "Amorphous-Nanocrystalline Fluorinated Halide Electrolytes With High Ionic Conductivity and High-Voltage Stability," *Journal of the American Chemical Society* 147, no. 18 (2025): 15136–15145.

22. Z. L. Dong, Y. Gan, V. Martins, et al., "Novel Sulfide-Chloride Solid-State Electrolytes With Tunable Anion Ratio for Highly Stable Solid-State Sodium-Ion Batteries," *Advanced Materials* 37, no. 30 (2025): 2503107.

23. L. Zhou, J. D. Bazak, C. Li, and L. F. Nazar, "4 V Na Solid State Batteries Enabled by a Scalable Sodium Metal Oxyhalide Solid Electrolyte," *ACS Energy Letters* 9, no. 8 (2024): 4093–4101.

24. F. Li, T. Liu, T. Wang, A. Wang, J. Wang, and Y. Yang, "Understanding Yielding and the Unusual Ductile-Brittle-Ductile Transition in Fe-Based Amorphous Nanocrystalline Alloy: A Combined Micromechanical and

Thermodynamic Study," *Journal of the Mechanics and Physics of Solids* 132 (2019): 103681.

25. H. Fang, Y. Pan, B. Wu, C. Lu, W. Ouyang, and Z. Liu, "Diffusion-Mediated Superelongation in Metal Nanorods," *Physical Review Letters* 132, no. 25 (2024): 256201.

26. E. Ruoff, S. Kmiec, and A. Manthiram, "Enhanced Interfacial Conduction in Low-Cost $NaAlCl_4$ Composite Solid Electrolyte for Solid-State Sodium Batteries," *Advanced Energy Materials* 14, no. 37 (2024): 2402091.

27. B. Wang, Y. Yang, Q. Xu, et al., "Thermal Stability Assessment of Sodium Solid Electrolytes," *Advanced Energy Materials* 16, no. 14 (2026): 06749.

28. R. Fehrmann, J. H. Von Barner, N. J. Bjerrum, and O. F. Nielsen, "Chloro Complexes in Molten Salts. 8. Potentiometric and Raman Spectroscopic Study of the Systems Sodium-Chloride-Aluminum Chloride, Sodium Chloride-Aluminum Chloride-Sodium Oxide, Sodium Chloride-Aluminum Chloride-Selenium Tetrachloride, and Sodium Chloride-Aluminum Chloride-Selenium Tetrachloride-Sodium Oxide," *Inorganic Chemistry* 20, no. 6 (1981): 1712–1718.

29. V. A. Elterman, P. Y. Shevelin, L. A. Yolshina, E. G. Vovkotrub, and A. V. Borozdin, "Effects of $AlCl_3$–1-Ethyl-3-Methylimidazolium Chloride Ionic Liquid Composition on Transport Properties," *Journal of Molecular Liquids* 320 (2020): 114482.

30. R. W. Berg, "Ab Initio MO Calculations on the Structure and Raman and Infrared Spectra of $[Al_4O_2Cl_{10}]^{2-}$ Oxide in Chloroaluminate Melts," *Zeitschrift für Naturforschung A* 62, no. 3–4 (2007): 157–168.

31. M.-A. Einarsrud, E. Rytter, and M. Ystenes, "Experimental and Theoretical Spectra of Stoichiometric Complex Ions in Oxochloroaluminate Melts," *Vibrational Spectroscopy* 1, no. 1 (1990): 61–68.

32. I. You, B. Singh, M. Cui, et al., "A Facile Route to Plastic Inorganic Electrolytes for All-Solid State Batteries Based on Molecular Design," *Energy & Environmental Science* 18, no. 1 (2025): 478–491.

33. T. Strässle, S. Klotz, K. Kunc, V. Pomjakushin, and J. S. White, "Equation of State of Lead From High-Pressure Neutron Diffraction up to 8.9 GPa and Its Implication for the NaCl Pressure Scale," *Physical Review B* 90, no. 1 (2014): 014101.

34. C. J. Nicholls and D. S. Urch, "A Study of the Bonding in Some Compounds of Aluminium Using Al-$K\beta_{1,3}$ X-Ray Emission Spectra," *Journal of the Chemical Society, Dalton Transactions* 3, no. 9 (1974): 901–907.

35. Z. Wang, C. Li, L. Liu, and T.-K. Sham, "Probing Defect Emissions in Bulk, Micro- and Nano-Sized α-Al_2O_3 via X-Ray Excited Optical Luminescence," *The Journal of Chemical Physics* 138, no. 8 (2013): 084706.

36. X. Xu, Q. Gao, L. Tang, and W. Chen, "Structural Determination of Amorphous $AlCl_{3-x}Na_2O$ Solid Electrolytes," *Applied Physics Letters* 126, no. 17 (2025): 171903.

37. B. Krebs, H. Greiwing, C. Brendel, F. Taulelle, M. Gaune-Escard, and R. W. Berg, "ChemInform Abstract: Crystallographic and ^{27}Al NMR Study on Premelting Phenomena in Crystals of Sodium Tetrachloroaluminate," *ChemInform* 22, no. 23 (1991): 981–988.

38. M. Uda, D. Yamashita, D. Terashi, et al., "XANES Spectra of Sesqui-Oxides of Al, Cr and Fe," *Journal of Electron Spectroscopy and Related Phenomena* 114–116 (2001): 819–823.

39. T. Krahl, R. Stösser, E. Kemnitz, et al., "Structural Insights Into Aluminum Chlorofluoride (ACF)," *Inorganic Chemistry* 42, no. 20 (2003): 6474–6483.

40. X. Lin, S. Zhang, M. Yang, et al., "A Family of Dual-Anion-Based Sodium Superionic Conductors for All-Solid-State Sodium-Ion Batteries," *Nature Materials* 24 (2024): 83–91.

41. H. Wang, F. Ding, Y. Wang, et al., "In Situ Plastic-Crystal-Coated Cathode Toward High-Performance Na-Ion Batteries," *ACS Energy Letters* 8, no. 3 (2023): 1434–1444.

42. Z. Lian, H. Wang, Z. Chen, et al., "High-Energy Na-Ion Batteries Using Single-Crystalline Cathode," *ACS Energy Letters* 10 (2025): 1517–1528.

43. T. H. Wan, M. Saccoccio, C. Chen, and F. Ciucci, "Influence of the Discretization Methods on the Distribution of Relaxation Times Deconvolution: Implementing Radial Basis Functions With DRTtools," *Electrochimica Acta* 184 (2015): 483–499.

44. Y. Liu, H. Mao, R. Bai, et al., "Designing an Isotropic Epilayer for Stable 4.2 V Solid-State Na Batteries," *Nature Energy* 10 (2025): 1305–1314.

45. D. Y. Semerukhin, A. V. Kubarkov, V. G. Sergeyev, O. A. Semenikhin, and E. V. Antipov, "Analysis of the Distribution of Relaxation Times (DRT) Responses of Li-Ion Cells as a Function of Their Preparation Conditions," *Electrochimica Acta* 486 (2024): 144092.

46. C. Yang, J. Wang, C. Sang, et al., "In Situ Engineering of a Multifunctional Cathode–Electrolyte Interphase for Advanced Sodium-Ion Batteries," *ACS Energy Letters* 10, no. 7 (2025): 3544–3553.

47. Y. Gan, P. Ping, J. Wang, Y. Song, and W. Gao, "Comparative Analysis of Thermal Stability and Electrochemical Performance of $NaNi_{1/3}Fe_{1/3}Mn_{1/3}O_2$ Cathode in Different Electrolytes for Sodium Ion Batteries," *Journal of Power Sources* 594 (2024): 234008.

48. Q. Yang, J. Xu, X. Fu, et al., "Atomic Insight Into Li^+ Ion Transport in Amorphous Electrolytes $Li_xAlO_yCl_{3+x-2y}$ ($0.5 \leq x \leq 1.5$, $0.25 \leq y \leq 0.75$)," *Journal of Materials Chemistry A* 13, no. 3 (2025): 2309–2315.

49. G. Kresse and J. Furthmüller, "Efficient Iterative Schemes for Ab Initio Total-Energy Calculations Using a Plane-Wave Basis Set," *Physical Review B* 54, no. 16 (1996): 11169–11186.

50. J. P. Perdew, K. Burke, and M. Ernzerhof, "Generalized Gradient Approximation Made Simple," *Physical Review Letters* 77, no. 18 (1996): 3865–3868.

51. G. Kresse and J. Furthmüller, "Efficiency of Ab-Initio Total Energy Calculations for Metals and Semiconductors Using a Plane-Wave Basis Set," *Computational Materials Science* 6, no. 1 (1996): 15–50.

52. J. P. Perdew, M. Ernzerhof, and K. Burke, "Rationale for Mixing Exact Exchange With Density Functional Approximations," *Journal of Chemical Physics* 105, no. 22 (1996): 9982–9985.

Supporting Information

Additional supporting information can be found online in the Supporting Information section.

Supporting File: adma74493-sup-0001-SuppMat.docx.